

Article

Evaluating the Sorption Affinity of Low Specific Activity ^{99}Mo on Different Metal Oxide Nanoparticles

Mohamed F. Nawar ^{1,2,*} , Alaa F. El-Daoushy ² , Ahmed Ashry ³ , Mohamed A. Soliman ^{3,4} 
and Andreas Türler ¹ 

¹ Department of Chemistry, Biochemistry, and Pharmaceutical Sciences, Faculty of Science, University of Bern, Freiestrasse 3, CH-3012 Bern, Switzerland

² Radioactive Isotopes and Generators Department, Hot Laboratories Center, Egyptian Atomic Energy Authority, Cairo 13759, Egypt

³ Radiation Protection and Civil Defense Department, Nuclear Research Center, Egyptian Atomic Energy Authority, Cairo 13759, Egypt

⁴ Egypt Second Research Reactor, Nuclear Research Center, Egyptian Atomic Energy Authority, Cairo 13759, Egypt

* Correspondence: mohamed.nawar@unibe.ch

Abstract: $^{99}\text{Mo}/^{99\text{m}}\text{Tc}$ generators are mainly produced from ^{99}Mo of high specific activity generated from the fission of ^{235}U . Such a method raises proliferation concerns. Alternative methods suggested the use of low specific activity (LSA) ^{99}Mo to produce $^{99\text{m}}\text{Tc}$ generators. However, its applicability is limited due to the low adsorptive capacity of conventional adsorbent materials. This study attempts to investigate the effectiveness of some commercial metal oxides nanoparticles as adsorbents for LSA ^{99}Mo . In a batch equilibration system, we studied the influence of solution pH (from 1–8), contact time, initial Mo concentration (from 50–500 $\text{mg}\cdot\text{L}^{-1}$), and temperature (from 298–333 K). Moreover, equilibrium isotherms and thermodynamic parameters (changes in free energy ΔG^0 , enthalpy change ΔH^0 , and entropy ΔS^0) were evaluated. The results showed that the optimum pH of adsorption ranges between 2 and 4, and that the equilibrium was attained within the first two minutes. In addition, the adsorption data fit well with the Freundlich isotherm model. The thermodynamic parameters prove that the adsorption of molybdate ions is spontaneous. Furthermore, some investigated adsorbents showed maximum adsorption capacity ranging from 40 ± 2 to 73 ± 1 $\text{mg Mo}\cdot\text{g}^{-1}$. Therefore, this work demonstrates that the materials used exhibit rapid adsorption reactions with LSA ^{99}Mo and higher capacity than conventional alumina ($2\text{--}20$ $\text{mg Mo}\cdot\text{g}^{-1}$).

Keywords: LSA ^{99}Mo ; thermodynamic parameters; solid-phase extraction; isotherm; metal oxides NPs



Citation: Nawar, M.F.; El-Daoushy, A.F.; Ashry, A.; Soliman, M.A.; Türler, A. Evaluating the Sorption Affinity of Low Specific Activity ^{99}Mo on Different Metal Oxide Nanoparticles. *Inorganics* **2022**, *10*, 154. <https://doi.org/10.3390/inorganics10100154>

Academic Editor: Roberto Nisticò

Received: 7 August 2022

Accepted: 23 September 2022

Published: 26 September 2022

Publisher's Note: MDPI stays neutral with regard to jurisdictional claims in published maps and institutional affiliations.



Copyright: © 2022 by the authors. Licensee MDPI, Basel, Switzerland. This article is an open access article distributed under the terms and conditions of the Creative Commons Attribution (CC BY) license (<https://creativecommons.org/licenses/by/4.0/>).

1. Introduction

$^{99}\text{Mo}/^{99\text{m}}\text{Tc}$ radioisotope generators have a growing importance in nuclear medicine investigations. They are the primary source of supplying $^{99\text{m}}\text{Tc}$ radionuclide for diagnostic purposes [1–3]. $^{99\text{m}}\text{Tc}$ is considered the workhorse of all nuclear medicine applications [4,5]. It is involved in more than 80% of all in vivo diagnostic procedures because of its ideal nuclear characteristics, such as the short half-life of 6 h, absence of beta particles, and emission of a mono-energetic photon with low energy at 140 keV [3,6]. Therefore, this leads to less radiation exposure dose to the patients, and it produces a high-quality image for better diagnosis aspects. Furthermore, its unique labeling chemistry allows the use of a wide range of $^{99\text{m}}\text{Tc}$ -labelled compounds to visualize different body organs [7,8]. For instance, $^{99\text{m}}\text{Tc}$ -DTPA and $^{99\text{m}}\text{Tc}$ -MAG3 are used to monitor renal functions [9]. In addition, $^{99\text{m}}\text{Tc}$ -tetrofosmin, $^{99\text{m}}\text{Tc}$ -sestamibi, and $^{99\text{m}}\text{Tc}$ -teboroxime are utilized for the diagnosis of cardiac disease [10]. Moreover, $^{99\text{m}}\text{Tc}$ -lidofenin is applied for liver diagnostics [11]. Furthermore, $^{99\text{m}}\text{Tc}$ -medronate, $^{99\text{m}}\text{Tc}$ -propyleneamineoxime, and $^{99\text{m}}\text{Tc}$ -MDP (methylene

diphosphonate) are involved in skeletal imaging, cerebral perfusion, and diagnosis of bone metastases, respectively [12–15].

Among the developed $^{99}\text{Mo}/^{99\text{m}}\text{Tc}$ generators, the chromatographic column type is the most widely used system [3,16]. This system is based on adsorbing ^{99}Mo on a column filled with a suitable material from which $^{99\text{m}}\text{TcO}_4^-$ can be easily eluted while ^{99}Mo remains adsorbed [3]. The differences between these generators include the column material and the origin of the parent, ^{99}Mo . The main practical difficulties linked to the preparation of $^{99}\text{Mo}/^{99\text{m}}\text{Tc}$ generators are the low sorption capacity of the bulk conventional inorganic sorbents usually used. These sorbents have low sorption capacity (2–20 mg Mo/g) due to the low availability of active sites and relatively limited surface area [3]. Consequently, such sorbents require a parent of high specific activity to prepare a useful generator of a proper radioactivity level. A high specific activity parent can be produced from the fission of ^{235}U . Fission-produced ^{99}Mo faces some critical difficulties. For example, sophisticated infrastructures and well-qualified personnel are needed to separate and purify ^{99}Mo from the irradiated ^{235}U target and other fission products. In addition, a considerable level of radioactive waste is generated during the manufacturing process, which increases the cost of production [17,18]. Alternatively, research studies focused on developing clinical-grade chromatographic $^{99}\text{Mo}/^{99\text{m}}\text{Tc}$ generators based on ^{99}Mo of low specific activity (LSA) [3,19,20]. However, this proposal demands using high-capacity sorbents to compensate for the LSA ^{99}Mo and make it more reliable from the economic point of view [17,21].

The use of advanced nanomaterials has generated a growing interest in developing diagnostic $^{99\text{m}}\text{Tc}$ generators [3]. Nawar and Türler [3] highlighted several nanomaterial adsorbents that have been developed for $^{99}\text{Mo}/^{99\text{m}}\text{Tc}$ generator application. This class of sorbents possesses appreciable adsorption capacity and unique performance [20]. In this regard, the utilization of advanced commercial metal-oxide nanoparticles is an exciting idea due to their improved properties. In contrast to traditional sorbents, these nano-adsorbents have large surface-to-volume ratios, enhanced porosity, improved surface reactivity, and significant radiation resistance and chemical stability [21,22]. Therefore, they show high adsorption efficiency and selectivity [23].

In this study, we intend to evaluate the sorption efficiency of some commercially available nano-metal oxides towards LSA ^{99}Mo . To achieve this goal, we investigated the adsorption behavior of the selected materials for LSA ^{99}Mo under different experimental conditions. These conditions include the pH, initial concentration of molybdate ions, contact time, and temperature. In addition, to better understand their sorption behavior, the sorption kinetics, equilibrium isotherms, and thermodynamic behavior were evaluated.

2. Results and Discussion

2.1. Effect of Solution pH

The solution pH has a profound impact on the efficiency of the adsorption process. The influence of pH can be clarified by understanding its role in varying the ionic state of the functional groups on the adsorbent surface. Moreover, it affects the ionization and/or the dissociation of the studied ions [24]. In this context, a batch equilibration experiment was conducted at a pH range from 1 to 8 to determine the optimum pH value that shows the maximum ^{99}Mo retention on each adsorbent. Figure 1a depicts the distribution coefficients (K_d) of $\text{CA-}^{99}\text{Mo}$ at different pH values. The data presented in this figure show that higher K_d values are observed at pH values (2–4). Beyond this region, the K_d values decrease with increasing the solution pH, which agrees with previously published studies [25].

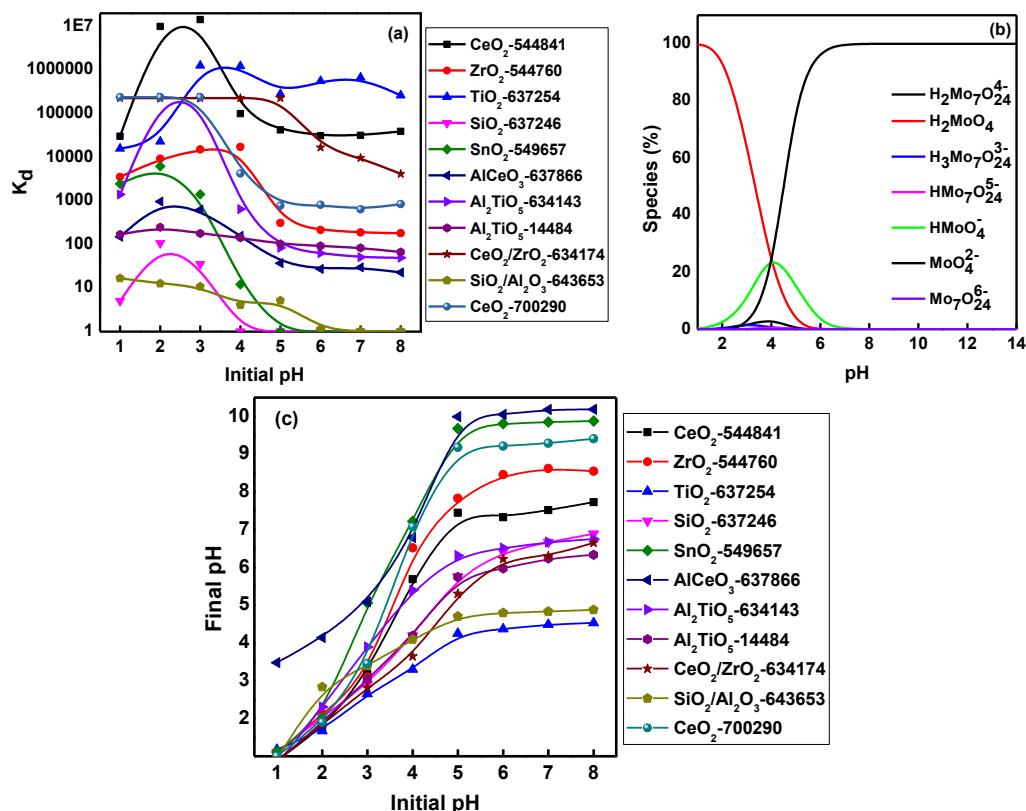
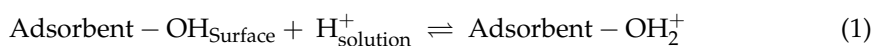
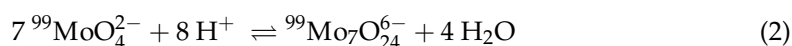


Figure 1. Effect of initial pH on (a) the distribution coefficients (K_d) of CA-⁹⁹Mo on different metal oxides NPs ($C_0 = 50 \text{ mg}\cdot\text{L}^{-1}$, $V/m = 100 \text{ mL}\cdot\text{g}^{-1}$, and temperature = $298 \pm 1 \text{ K}$), (b) Speciation of molybdenum [22], and (c) variation of the final pH values.

Since the adsorbents are metal oxides, they might have similar surface chemistry. Moreover, since the adsorption process depends mainly on the aqueous phase's pH values and the adsorbent material's surface characteristics, we investigated the isoelectric point (pH_{IEP}) of each adsorbent (Table 1). The pH_{IEP} measurements help to clarify the sorption mechanism. The sorbent surface carries a positive charge at $\text{pH} < \text{pH}_{\text{IEP}}$, zero charge at $\text{pH} \sim \text{pH}_{\text{IEP}}$, and is negatively charged at $\text{pH} > \text{pH}_{\text{IEP}}$. Consequently, there is a change in the pH_{IEP} of the sorbent with the pH of an aqueous solution. Nawar et al. [22] reported that this behavior might occur because amphoteric hydroxyl groups cover the adsorbent surface. Hence, based on the pH of the medium, these groups develop different reactions in different pH media, resulting in positive or negative charges appearing on the adsorbent surface. Herein, at $\text{pH} < \text{pH}_{\text{IEP}}$, they are protonated, and the surface develops a positive charge as follows:



The data presented in Figure 1a can be interpreted by considering the speciation diagram of molybdenum shown in Figure 1b [22]. The speciation data are generated using the PHREEQC software (version 3) to determine the predominant Mo species at different pHs for the following conditions: $C_0 = 50 \text{ mg}\cdot\text{L}^{-1}$ at 298 K and using the built-in database of stability constants [22]. At acidic medium, the molybdate anionic species exist and polymerize, increasing the molybdenum content per unit charge as follows:



Consequently, this results in favorable interactions between negatively charged molybdenum polyanions and positively charged adsorbents surfaces [26]. At higher pH values,

the speciation shifts to less negatively charged Mo species, and the density of hydroxyl groups (OH^-) increases in solution. These hydroxyl anions compete with less negatively charged molybdenum anions to retain the available active sites on adsorbents surfaces, explaining the low K_d distribution values at higher pH values [22,27].

Table 1. Description of the analyzed commercial metal oxides NPs *.

No.	Name	Description	Particle Size, (nm)	Surface Area, ($\text{m}^2 \cdot \text{g}^{-1}$)	Isoelectric Point (pH_{IEP})
CeO ₂ -544841	Cerium oxide-SA-544841	Molecular formula: CeO ₂ Molecular weight: 172.11 Density: 7.13 g·mL ⁻¹ at 298 K	<25	N.A	5
ZrO ₂ -544760	Zirconium oxide-SA-544760	Molecular formula: ZrO ₂ Molecular weight: 123.22 Density: 5.89 g·mL ⁻¹ at 298 K	<100	≥25	6.1
TiO ₂ -637254	Titanium oxide-SA-637254	Molecular formula: TiO ₂ Molecular weight: 79.87 Density: 3.9 g·mL ⁻¹ at 298 K	<25	45–55	6.6
SnO ₂ -549657	Tin oxide-SA-549657	Molecular formula: SnO ₂ Molecular weight: 150.71 Density: 6.95 g·mL ⁻¹ at 298 K	≤100	20.1	3.8
SiO ₂ -637246	Silicon oxide-SA-637246	Molecular formula: SiO ₂ Molecular weight: 60.08 Density: 2.2–2.6 g·mL ⁻¹ at 298 K	5–20	590–690	2.5
AlCeO ₃ -637866	Cerium aluminium oxide-SA-637866	Molecular formula: AlCeO ₃ Molecular weight: 215.1	≤80	N.A	4.8
Al ₂ TiO ₅ -634143	Aluminium titanium oxide-SA-634143	Molecular formula: Al ₂ TiO ₅ Molecular weight: 181.83	<25	N.A	6.4
Al ₂ TiO ₅ -14484	Aluminium titanium oxide-AA-14484	Molecular formula: Al ₂ TiO ₅ Molecular weight: 181.86	100 mesh	N.A	6.5
CeO ₂ /ZrO ₂ -634174	Cerium zirconium oxide-SA-634174	Molecular formula: (CeO ₂)·(ZrO ₂) Molecular weight: 295.34 Density: 6.61 g·mL ⁻¹ at 298 K	<50	N.A	6.7
SiO ₂ /Al ₂ O ₃ -643653	Aluminosilicate-SA-643653	Molecular formula: (SiO ₂) _x (Al ₂ O ₃) _y pore volume: 0.8–1.1 cm ³ ·g ⁻¹ mesostructured, pore size: 2–4 nm	4.5–4.8	900–1100	6
CeO ₂ -700290	Cerium oxide-SA-700290	Molecular formula: CeO ₂ Molecular weight: 172.11 Density: 7.13 g·mL ⁻¹ at 298 K	<50	30	4.5

* The information was provided by the supplier. Only the isoelectric point data were determined experimentally. Abbreviations: AA: Alfa Aesar (Kandel, Germany); N.A: Not Available; SA: Sigma-Aldrich (Buchs, Switzerland).

Moreover, based on the isoelectric point (pH_{IEP}) of each sorbent material (Table 1) and the measured final solution pH (Figure 1c), it can be observed that K_d values start to decrease when the final solution pH exceeds the sorbent's pH_{IEP} , which can be attributed to the expected change in the surface charge of the sorbent material. As previously mentioned, at solution pH values above the pH_{IEP} , the sorbent surface becomes predominately negatively charged. As a result, repulsion between the negatively charged sorbent surface

and the negatively charged molybdenum polyanions takes place, leading to the observed decrease in K_d values [22,28].

It can also be observed that both silicon oxide and aluminosilicate nanoparticles possess small particle sizes (5–20 and 4.5–4.8 nm) and high surface area (590–690 and 900–1100 $\text{m}^2 \cdot \text{g}^{-1}$), respectively (Table 1). However, both adsorbents show a weak affinity for Mo species. This behavior may be attributed to their poor stability with increasing pH values. At high pH values, the dissolution of silica occurs, resulting in the formation of monomeric ortho-silicic acid (H_4SiO_4), which can be explained due to the presence of more hydroxyl groups. These hydroxyl groups are chemisorbed on the adsorbent surface, which increases the number of coordination bonds around the silicon atom to more than four bonds. Consequently, it may lead to Si-O bond rupture, and the silicon atom dissolves as $\text{Si}(\text{OH})_4$ and ortho-silicic acid [29].

According to the obtained results, we selected six adsorbents that showed high distribution coefficient values towards CA^{99}Mo for the subsequent investigations. These adsorbents are CeO_2 -544841, ZrO_2 -544760, TiO_2 -637254, Al_2TiO_5 -634143, $\text{CeO}_2/\text{ZrO}_2$ -634174, and CeO_2 -700290.

2.2. Adsorption Isotherm

Equilibrium isotherms are essential in describing the adsorption mechanisms for the interaction of Mo(VI) ions with the surfaces of the investigated metal oxides NPs. These mechanisms describe the adsorption process successfully. Here, we investigated equilibrium data obtained for adsorption of CA^{99}Mo on CeO_2 -544841, ZrO_2 -544760, TiO_2 -637254, Al_2TiO_5 -634143, $\text{CeO}_2/\text{ZrO}_2$ -634174, and CeO_2 -700290 with various isotherm models to find out which one is the most suitable for describing the obtained adsorption equilibrium data.

2.2.1. Freundlich Isotherm

Many studies have utilized the Freundlich adsorption isotherm model proposed as a general power equation used to describe the adsorption of radionuclides in a large number of studies [30–32]. The Freundlich isotherm has the form shown as follows:

$$q_e = K_f(C_e)^{\frac{1}{n_f}} \quad (3)$$

where q_e ($\text{mg} \cdot \text{g}^{-1}$) is the concentration of CA^{99}Mo adsorbed and C_e ($\text{mg} \cdot \text{L}^{-1}$) is the concentration of Mo remaining in the solution. K_f ($\text{mg}^{1-n_f} \cdot \text{L}^n \cdot \text{g}^{-1}$) and n_f (dimensionless) are constants unique to each combination of adsorbent and adsorbate.

2.2.2. Langmuir Isotherm

Langmuir (1918) developed an equation to describe the adsorption of gases on a solid surface that was subsequently adapted to describe the adsorption of solutes onto solids in aqueous solutions [31,33,34], as shown in Equation (4):

$$q_e = \frac{n_L K_L C_e}{1 + K_L C_e} \quad (4)$$

where q_e ($\text{mg} \cdot \text{g}^{-1}$) is the total concentration of solute adsorbed, K_L ($\text{L} \cdot \text{mg}^{-1}$) is an equilibrium constant, and n_L ($\text{mg} \cdot \text{g}^{-1}$) is the adsorption capacity.

Figure 2 presents the experimental adsorption equilibrium data obtained for Mo ions on the investigated metal oxide adsorbents as a plot of adsorption equilibrium capacity (q_e) against initial concentration (C_0). It is observed that there is an increase in the amount of Mo ions taken up with the increase in the initial metal ion concentration. This increase in the adsorbate uptake can be explained by the driving force for mass transfer [34].

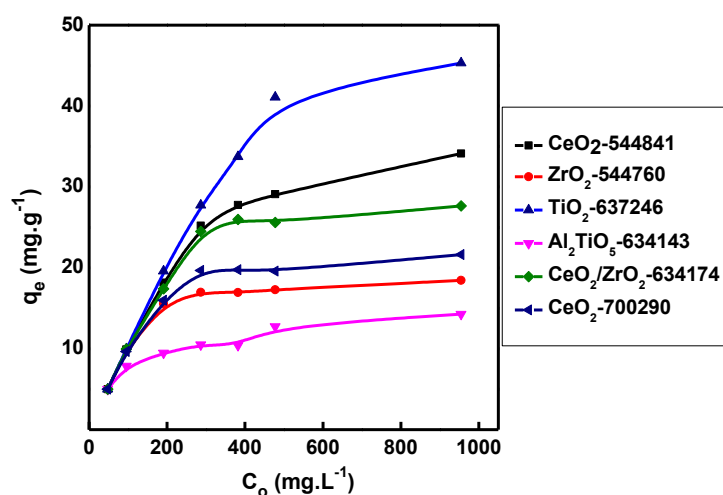


Figure 2. The influence of initial molybdate concentration on the equilibrium sorption capacity (q_e) of CA-⁹⁹Mo on different metal oxides NPs (pH = 3, V/m = 100 mL·g⁻¹, t = 24 h, and temperature = 298 ± 1 K).

The non-linear forms of both isotherm models were applied to the measured adsorption data (C_e versus q_e), and the data were displayed in Figure 3. Adsorption parameters were optimized using the add-ins “Solver” function in Microsoft Excel. Table 2 gives the Freundlich parameters (K_f and n_f), Langmuir parameters (K_L and n_L), and the goodness of fit of the model lines to the experimental data (R^2). Based on the regression coefficient values reported in Table 2, it is observed that good to excellent correlations between the experimental results and the fitted data of the Freundlich isotherm model were obtained for all the investigated sorbents. In contrast, the Langmuir model failed to fit any equilibrium sorption isotherm of the CA-⁹⁹Mo on all tested adsorbents; lower R^2 values were obtained.

These findings suggest that CA-⁹⁹Mo adsorption on metal oxide nanomaterials under investigation mainly occurred through multilayer adsorption at heterogeneous surfaces [31,35]. The Freundlich adsorption constant (n_f) is usually used as a measure of adsorption intensity as follows; (i) $n_f < 1$ indicates that adsorption takes place via a chemical process, (ii) $n_f = 1$ shows linear adsorption, (iii) while $n_f > 1$ indicates physisorption [35]. The n_f values displayed in Table 2 were higher than 1, indicating that CA-⁹⁹Mo adsorption on the materials used in this study was physisorption and favorable under the investigated conditions. Furthermore, the closer the $1/n$ value to 0 than unity (ranging from 0.10 to 0.25), the more heterogeneous the surface is, implying a broad distribution of adsorption sites on the adsorbent surface [32,33].

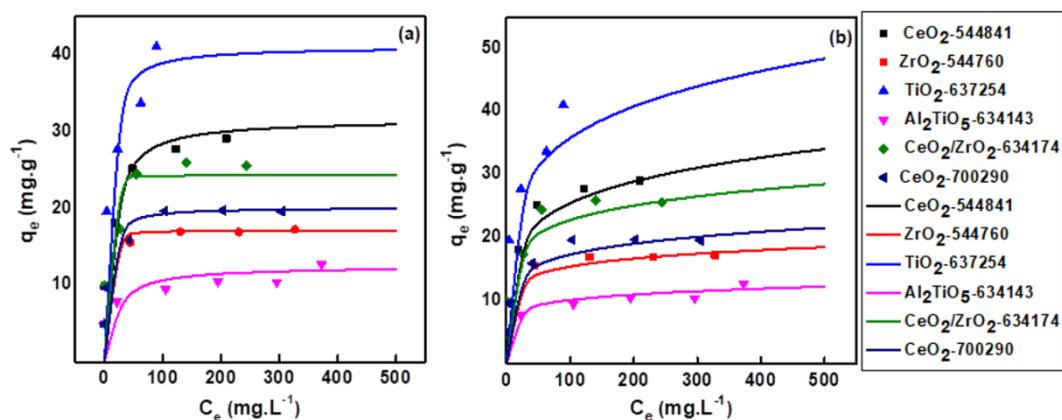


Figure 3. Adsorption isotherms: (a) Langmuir and (b) Freundlich of CA-⁹⁹Mo on different metal oxides NPs.

Table 2. Isotherm parameters calculations for the adsorption of CA-⁹⁹Mo on different metal oxides NPs.

Isotherm Model	Parameter	CeO ₂ -544841	ZrO ₂ -544760	TiO ₂ -637254	Al ₂ TiO ₅ -634143	CeO ₂ /ZrO ₂ -634174	CeO ₂ -700290
Langmuir	n _L (mg·g ⁻¹)	26.704	16.814	36.980	10.207	23.470	19.603
	K _L (L·mg ⁻¹)	0.407	0.993	0.311	0.0907	3.537	0.254
	R ²	0.911	0.957	0.930	0.836	0.870	0.954
Freundlich	$\frac{K_F}{(\text{mg}^{1-n} \text{L}^n \cdot \text{g}^{-1})}$	10.514	9.058	13.064	6.364	11.506	8.876
	n _f	5.010	8.294	4.079	10.325	6.346	6.644
	R ²	0.982	0.968	0.989	0.898	0.955	0.966

2.3. Thermodynamic Studies

We determined the amount of CA-⁹⁹Mo adsorbed on the surface of the materials investigated in the current study as a function of temperature (T) using adsorption thermodynamic parameters. These parameters include the Gibbs free energy ΔG^0 (kJ·mol⁻¹), the standard enthalpy change ΔH^0 (kJ·mol⁻¹), and the standard entropy change ΔS^0 (J·mol⁻¹·K⁻¹). They were investigated at different temperatures (298, 313, 323, and 333 K) using Equations (5) and (6) [34,36,37] and are tabulated in Table 3:

$$\Delta G^0 = -RT \ln K_d \quad (5)$$

$$\ln K_d = \frac{\Delta S^0}{R} - \frac{\Delta H^0}{RT} \quad (6)$$

where R is the universal gas constant (8.314 J·mol⁻¹·K⁻¹), T is the absolute temperature (K), and K_d (mL·g⁻¹) is the distribution coefficient.

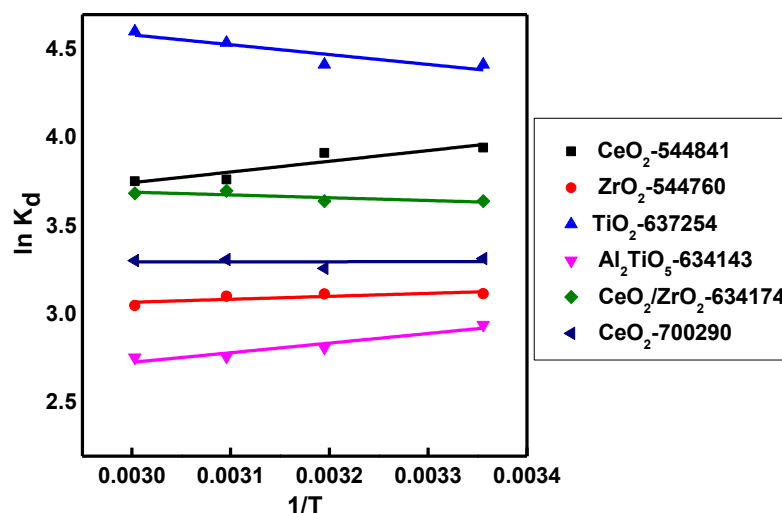
Table 3. Thermodynamic parameters for the sorption of CA-⁹⁹Mo on different metal oxides NPs.

Adsorbent	Temperature (K)	ΔG^0 (kJ·mol ⁻¹)	ΔH^0 (kJ·mol ⁻¹)	ΔS^0 (J·mol ⁻¹ ·K ⁻¹)
CeO ₂ -544841	298	-9.8 ± 2.9	-5.1 ± 1.5	16.0 ± 4.7
	313	-10.1 ± 3.0		
	323	-10.2 ± 3.0		
	333	-10.4 ± 3.1		
ZrO ₂ -544760	298	-7.8 ± 1.4	-1.4 ± 0.7	21.3 ± 2.2
	313	-8.1 ± 1.4		
	323	-8.3 ± 1.4		
	333	-8.5 ± 1.5		
TiO ₂ -637254	298	-10.9 ± 3.1	4.7 ± 1.5	52.0 ± 5.0
	313	-11.7 ± 3.1		
	323	-12.2 ± 3.2		
	333	-12.7 ± 3.2		
Al ₂ TiO ₅ -634143	298	-7.2 ± 2.0	-4.5 ± 1	9.1 ± 3.2
	313	-7.4 ± 2.0		
	323	-7.5 ± 2.0		
	333	-7.6 ± 2.0		

Table 3. Cont.

Adsorbent	Temperature (K)	ΔG^0 (kJ·mol ⁻¹)	ΔH^0 (kJ·mol ⁻¹)	ΔS^0 (J·mol ⁻¹ ·K ⁻¹)
CeO ₂ /ZrO ₂ -634174	298	-9.0 ± 1.4	1.3 ± 0.7	34.6 ± 2.2
	313	-9.5 ± 1.4		
	323	-9.9 ± 1.4		
	333	-10.2 ± 1.4		
CeO ₂ -700290	298	-8.2 ± 1.9	-0.1 ± 0.9	27.2 ± 3.0
	313	-8.6 ± 1.9		
	323	-8.9 ± 2.0		
	333	-9.1 ± 2.0		

Figure 4 shows linear plots of $\ln K_d$ versus $(1/T)$. The calculated ΔG^0 values at each temperature for all nano-adsorbents are $\Delta G^0 < 0$, which implies that the Mo(VI) adsorption process on the surfaces of all adsorbents is spontaneous and the reaction is feasible. Likewise, ΔG^0 values decrease with increasing temperature, indicating that the degree of spontaneity can be enhanced by increasing the temperature. Furthermore, the adsorption process is physisorption ($-20 < \Delta G^0 < 0$) [38]. The positive values of ΔS^0 ($\Delta S^0 > 0$) report random adsorption reactions of CA-⁹⁹Mo at all adsorbents surfaces. The values of ΔH^0 are positive ($\Delta H^0 > 0$) for both TiO₂-637254 and CeO₂/ZrO₂-634174, implying that CA-⁹⁹Mo adsorption at their surfaces is endothermic [39]. While for CeO₂-544841, ZrO₂-544760, Al₂TiO₅-634143, and CeO₂-700290, the change in enthalpy (ΔH^0) is negative ($\Delta H^0 < 0$), indicating that the adsorption of CA-⁹⁹Mo at their surfaces is exothermic [38,40].

Figure 4. Van't Hoff plot for the sorption of CA-⁹⁹Mo on different metal oxides NPs.

2.4. Determining the Maximum Sorption Capacity

In order to evaluate the maximum sorption capacity of each adsorbent, the equilibrations of CA-⁹⁹Mo with each adsorbent were performed separately. Batch equilibrations were repeated until no further ⁹⁹Mo(IV) uptake was observed, and the adsorbents became fully saturated with ⁹⁹Mo. After each equilibration, 1 mL aliquot was decanted, centrifuged, and counted. Ultimately, the maximum sorption capacity (q_{\max}) for each material was calculated by applying the following equation:

$$q_{\max} = \frac{\sum U\%}{100} \times C_o \times \frac{V}{m} \quad (\text{mg} \cdot \text{g}^{-1}) \quad (7)$$

where $U\%$ is the uptake percent of $CA-^{99}\text{Mo}$, $C_0(\text{mg}\cdot\text{L}^{-1})$ is the starting Mo(IV) concentration, V (L) is the liquid phase volume, and m (g) is the adsorbent weight. Figure 5 shows $CA-^{99}\text{Mo}$ maximum sorption capacity on different studied metal oxides NPs. It can be concluded that the studied metal oxide NPs show better sorption capacity than conventional alumina currently used in $^{99}\text{Mo}/^{99\text{m}}\text{Tc}$ generators. Nonetheless, the obtained capacities are insufficient for developing a clinical-grade $^{99\text{m}}\text{Tc}$ generator based on LSA ^{99}Mo .

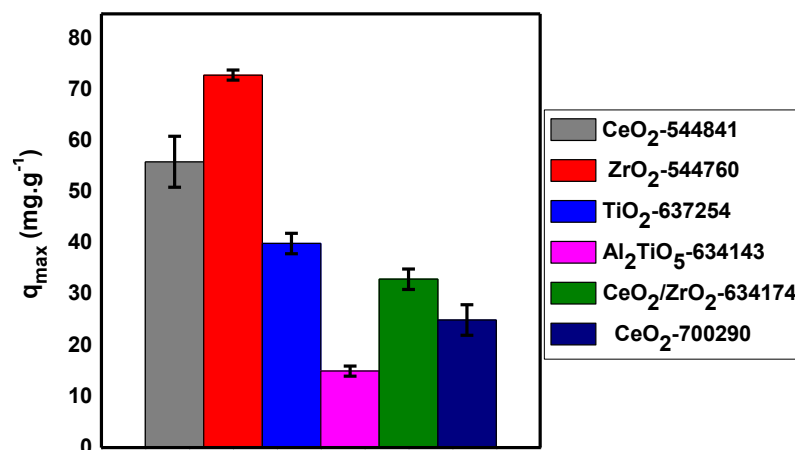


Figure 5. The maximum sorption capacity of different metal oxide NPs for $CA-^{99}\text{Mo}$.

2.5. Effect of Contact Time

The effect of contact time on the uptake percent of $CA-^{99}\text{Mo}$ was monitored for an initial Mo(IV) concentration of $50 \text{ mg}\cdot\text{L}^{-1}$ ($\text{pH}\sim 3$), using an adsorbent dose of 200 mg . The reaction temperature was adjusted to $298 \pm 1 \text{ K}$. The results are shown in Figure 6. The results show that the Mo uptake sharply increased at the beginning of the adsorption process and reached a constant value (a plateau value) in the first two minutes. This behavior indicates a rapid and almost instantaneous removal of $CA-^{99}\text{Mo}$ from the solution, and a dynamic equilibrium is established under the given experimental conditions. In order to design an effective adsorption process, determining the kinetic parameters is crucial. The kinetic data shown in Figure 6 revealed that the equilibrium for adsorption of Mo on metal oxide nano-adsorbents is already reached at the very beginning of the adsorption process. Consequently, using the current methodology, such data cannot be modeled with adsorption kinetic models.

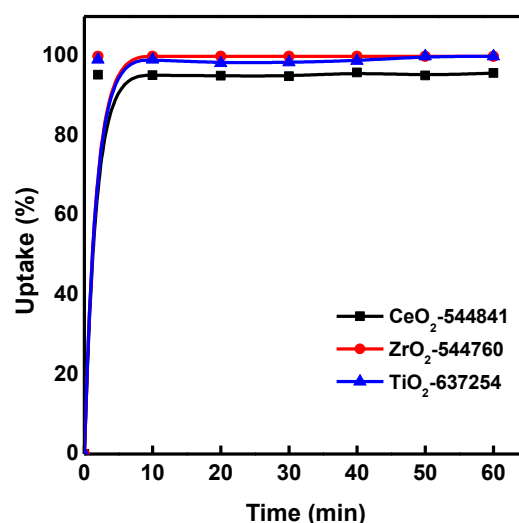


Figure 6. Effect of contact time on $CA-^{99}\text{Mo}$ uptake on different metal oxide NPs ($C_0 = 50 \text{ mg}\cdot\text{L}^{-1}$, $\text{pH} = 3$, $V/m = 100 \text{ mL}\cdot\text{g}^{-1}$, and temperature = $298 \pm 1 \text{ K}$).

3. Materials and Methods

3.1. Materials

All chemicals are of analytical grade purity (A. R. grade) and were used without further purification. Milli-Q water was used for the preparation of solutions and washings. Sodium hydroxide and nitric acid were purchased from Merck, Darmstadt, Germany. The metal oxide nanomaterials were purchased from different suppliers (Table 1).

^{99}Mo radiotracer solution was obtained by eluting a 40 GBq fission ^{99}Mo alumina-based $^{99}\text{Mo}/^{99\text{m}}\text{Tc}$ generator (Pertector, manufactured by National Centre for Nuclear Research, POLATOM, Otwock, Poland) with 5 mL of 1 M NaOH solution after ~7 d from the calibration date. The total ^{99}Mo radioactivity was measured with a Capintec Radioisotopes Calibrator (model CRC-55tR Capintec, Inc., Florham Park, NJ, USA). The ^{99}Mo eluate solution was passed through a 0.45 micro-Millipore filter to retain alumina particles. Then, the ^{99}Mo solution was treated with nitric acid to attain the desired pH value.

3.2. Batch Equilibrium Studies

A batch equilibration experiment was conducted to investigate the adsorption behavior of carrier-added (CA) ^{99}Mo (Mo(IV) treated with ^{99}Mo) on several commercial metal oxide nanoparticles (NPs) under different conditions. These conditions included the influence of pH, contact time, reaction temperature, and initial adsorbate concentration. In a series of clean glass bottles, we added 200 mg of each adsorbent to 20 mL of ^{99}Mo (IV) solution of a given concentration and pH value. Subsequently, the mixtures were shaken in a thermostatic shaker water bath (Julabo GmbH, Seelbach, Germany) at 298 ± 1 K for 24 h. Eventually, the supernatant solution was collected, centrifuged, and 1 mL was separated for radiometric measurements. For all radiometric identifications and γ -spectrometry, we used a multichannel analyzer (MCA) of Inspector 2000 model, Canberra Series, Mirion Technologies, Inc., Meriden, CT, USA, coupled with a high-purity germanium coaxial detector (HPGe). All samples have fixed geometry and were counted at a low dead time (<2%). The measurements were done by using an appropriate gamma-ray peak of 740 keV.

3.2.1. Distribution Ratio (K_d)

The distribution coefficient (K_d) values of CA- ^{99}Mo were investigated at a wide range of pH (from 1–8). For adjusting the desired pH value of the solutions, few drops of 0.5 M nitric acid or 0.5 M sodium hydroxide were added. The pH values of the solutions were measured before and after reaching the equilibrium state. pH values were determined using a pH-meter with a microprocessor (Mettler Toledo, Seven Compact S210 model, Greifensee, Switzerland).

3.2.2. Adsorption Isotherm

In order to determine the sorption isotherms, we used different initial molybdate ion concentrations from 50 to 500 $\text{mg}\cdot\text{L}^{-1}$ while keeping the adsorbent amount constant. Moreover, the solution pH, equilibrium time, and reaction temperature were kept at pH~3, 24 h, and 298 ± 1 K, respectively. In addition, the equilibrium adsorption capacity (q_e) was calculated. Finally, we used the obtained results to determine the sorption isotherm model.

3.2.3. Thermodynamic Studies

The reaction temperature effect on the uptake of carrier-added ^{99}Mo was studied at four different reaction temperatures (298, 313, 323, and 333 K). At each temperature, we added 20 mL of CA- ^{99}Mo solution (pH 3) in contact with 200 mg of the adsorbent material for 24 h. From the resulting data, we calculated different thermodynamic parameters, namely the standard enthalpy change (ΔH^0), standard entropy change (ΔS^0), and Gibbs free energy change (ΔG^0).

3.2.4. Effect of Contact Time

In order to investigate the ^{99}Mo adsorption rate on the studied metal oxides NPs, we monitored the progress of the uptake capacity of $^{99}\text{MoO}_4^{2-}$ ions ($50 \text{ mg}\cdot\text{L}^{-1}$ and $\text{pH}\sim 3$) at different time slots. The adsorption of $\text{CA-}^{99}\text{Mo}$ was followed with time until the equilibrium was established. Finally, we calculated the ^{99}Mo capacity (q_t) in $\text{mg}\cdot\text{g}^{-1}$ at each time (t).

3.3. Calculations

The adsorption data of $\text{CA-}^{99}\text{Mo}$ include uptake percent ($U\%$), distribution coefficient (K_d), equilibrium capacity (q_e), and equilibrium concentration (C_e). These data were calculated according to the following equations:

$$U\% = \frac{(A_i - A_f)}{A_i} \times 100 \quad (8)$$

$$q_e = \frac{U\%}{100} \times C_0 \times \frac{V}{m} \quad (\text{mg}\cdot\text{g}^{-1}) \quad (9)$$

$$C_e = A_i - \left(A_i \times \frac{U\%}{100} \right) \quad (\text{mg}\cdot\text{L}^{-1}) \quad (10)$$

$$K_d = \frac{A_i - A_f}{A_i} \times \frac{V'}{m} \quad (\text{mL}\cdot\text{g}^{-1}) \quad (11)$$

where A_i and A_f are the initial and final ^{99}Mo radioactivity in counts/min. C_0 ($\text{mg}\cdot\text{L}^{-1}$) is the initial concentration of $\text{CA-}^{99}\text{Mo}$, V (L) and V' (mL) represent the volume of liquid phases, and m (g) is the weight of the solid phase.

4. Summary and Conclusions

The main objective of this study was to evaluate the adsorption affinity of different commercial metal oxides NPs purchased from different suppliers towards $\text{LSA } ^{99}\text{Mo}$. All experiments were conducted at static equilibrium conditions. We studied the distribution ratio of $\text{CA-}^{99}\text{Mo}$ in a pH range of 1 to 8. The optimum adsorption pH was found to be in the range of pH 2 to 4. In addition, the Freundlich isotherm model fitted the experimental data of the $\text{CA-}^{99}\text{Mo}$ on all adsorbent materials investigated in this study. Moreover, we determined the values of enthalpy change (ΔH^0), entropy change (ΔS^0), and free energy change (ΔG^0) at the different reaction temperatures. Furthermore, the maximum adsorption capacities were evaluated, and the best adsorbents showed a capacity of 40 ± 2 to $73 \pm 1 \text{ mg Mo}\cdot\text{g}^{-1}$. Summing up the results, it can be concluded that the adsorption behavior of the materials investigated depends on the solution pH, contact time, initial metal ion concentration, and temperature. Furthermore, the investigated materials showed higher static sorption capacities than conventional alumina ($2\text{--}20 \text{ mg Mo}\cdot\text{g}^{-1}$). Nonetheless, they are not suitable to build a useful $^{99}\text{Mo}/^{99\text{m}}\text{Tc}$ generator using $\text{LAS } ^{99}\text{Mo}$ for radiopharmaceutical applications. Since the available specific activity of $\text{LAS } ^{99}\text{Mo}$ is $2.5\text{--}5 \text{ Ci/g Mo}$, approximately $20\text{--}25 \text{ g}$ of each material would be required to prepare a $^{99\text{m}}\text{Tc}$ generator of 37 GBq (1 Ci). Using such a massive amount of sorbent material per generator would deteriorate the elution performance and the radioactive concentration of the produced $^{99\text{m}}\text{Tc}$.

Author Contributions: Conceptualization, M.F.N.; methodology, M.F.N. and A.F.E.-D.; software, M.F.N., A.F.E.-D. and A.A.; validation, M.F.N., A.F.E.-D., A.A., M.A.S. and A.T.; formal analysis, M.F.N., A.F.E.-D. and A.A.; investigation, M.F.N.; data curation, M.F.N., A.F.E.-D. and A.T.; writing—original draft preparation, M.F.N.; writing—review and editing, A.F.E.-D., A.A., M.A.S. and A.T.; visualization, M.F.N. and A.F.E.-D.; supervision, A.T.; project administration, M.F.N. and A.T.; funding acquisition, M.F.N. All authors have read and agreed to the published version of the manuscript.

Funding: The research was funded by the Swiss National Science Foundation (grant number CR-SII5_180352). Mohamed F. Nawar gratefully acknowledges the funding support of the Swiss Government Excellence fellowships program (fellowship No: 2017.1028).

Institutional Review Board Statement: Not applicable.

Informed Consent Statement: Not applicable.

Data Availability Statement: Data is contained within the article.

Acknowledgments: The authors would like to express their sincere thanks to Marcel Langensand, Managing Director, Medeo AG, CH-5040 Schöftland, Switzerland, for his valuable support in supplying $^{99}\text{Mo}/^{99\text{m}}\text{Tc}$ generators to conduct this research study.

Conflicts of Interest: The authors declare no conflict of interest.

References

1. Cutler, C.S. Supply of Mo-99: Focus on U.S. supply. Trends in Radiopharmaceuticals (ISTR-2019). In Proceedings of the International Symposium, Vienna, Austria, 28 October–1 November 2019; International Atomic Energy Agency (IAEA): Vienna, Austria, 2020.
2. Munir, M.; Sriyono; Abidin; Sarmini, E.; Saptiama, I.; Kadarisman; Marlina. Development of mesoporous γ -alumina from aluminium foil waste for $^{99}\text{Mo}/^{99\text{m}}\text{Tc}$ generator. *J. Radioanal. Nucl. Chem. Artic.* **2020**, *326*, 87–96. [[CrossRef](#)]
3. Nawar, M.F.; Türler, A. New strategies for a sustainable $^{99\text{m}}\text{Tc}$ supply to meet increasing medical demands: Promising solutions for current problems. *Front. Chem.* **2022**, *10*, 926258. [[CrossRef](#)] [[PubMed](#)]
4. Capogni, M.; Pietropaolo, A.; Quintieri, L.; Angelone, M.; Boschi, A.; Capone, M.; Cherubini, N.; De Felice, P.; Dodaro, A.; Duatti, A.; et al. 14 MeV Neutrons for $^{99}\text{Mo}/^{99\text{m}}\text{Tc}$ Production: Experiments, Simulations and Perspectives. *Molecules* **2018**, *23*, 1872. [[CrossRef](#)] [[PubMed](#)]
5. Duatti, A. Review on $^{99\text{m}}\text{Tc}$ radiopharmaceuticals with emphasis on new advancements. *Nucl. Med. Biol.* **2021**, *92*, 202–216. [[CrossRef](#)] [[PubMed](#)]
6. Boschi, A.; Uccelli, L.; Martini, P. A Picture of Modern Tc-99m Radiopharmaceuticals: Production, Chemistry, and Applications in Molecular Imaging. *Appl. Sci.* **2019**, *9*, 2526. [[CrossRef](#)]
7. Mohan, A.-M.; Beindorff, N.; Brenner, W. Nuclear Medicine Imaging Procedures in Oncology. *Metastasis* **2021**, *2294*, 297–323. [[CrossRef](#)]
8. Kniess, T.; Laube, M.; Wüst, F.; Pietzsch, J. Technetium-99m based small molecule radiopharmaceuticals and radiotracers targeting inflammation and infection. *Dalton Trans.* **2017**, *46*, 14435–14451. [[CrossRef](#)] [[PubMed](#)]
9. Momin, M.; Abdullah, M.; Reza, M. Comparison of relative renal functions calculated with $^{99\text{m}}\text{Tc}$ -DTPA and $^{99\text{m}}\text{Tc}$ -DMSA for kidney patients of wide age ranges. *Phys. Med.* **2018**, *45*, 99–105. [[CrossRef](#)]
10. Fang, W.; Liu, S. New $^{99\text{m}}\text{Tc}$ Radiotracers for Myocardial Perfusion Imaging by SPECT. *Curr. Radiopharm.* **2019**, *12*, 171–186. [[CrossRef](#)]
11. Marlina, M.; Lestari, E.; Abidin, A.; Hambali, H.; Saptiama, I.; Febriana, S.; Kadarisman, K.; Awaludin, R.; Tanase, M.; Nishikata, K.; et al. Molybdenum-99 (^{99}Mo) Adsorption Profile of Zirconia-Based Materials for $^{99}\text{Mo}/^{99\text{m}}\text{Tc}$ Generator Application. *At. Indones.* **2020**, *46*, 91–97. [[CrossRef](#)]
12. Papagiannopoulou, D. Technetium-99m radiochemistry for pharmaceutical applications. *J. Label. Compd. Radiopharm.* **2017**, *60*, 502–520. [[CrossRef](#)] [[PubMed](#)]
13. Sharma, S.; Jain, S.; Baldi, A.; Singh, R.K.; Sharma, R.K. Intricacies in the approval of radiopharmaceuticals-regulatory perspectives and the way forward. *Curr. Sci.* **2019**, *116*, 47–55. [[CrossRef](#)]
14. Lassen, A.; Stokely, E.; Vorstrup, S.; Goldman, T.; Henriksen, J.H. Neuro-SPECT: On the development and function of brain emission tomography in the Copenhagen area. *Clin. Physiol. Funct. Imaging* **2021**, *41*, 10–24. [[CrossRef](#)]
15. Chen, B.; Wei, P.; Macapinlac, H.A.; Lu, Y. Comparison of ^{18}F -Fluciclovine PET/CT and $^{99\text{m}}\text{Tc}$ -MDP bone scan in detection of bone metastasis in prostate cancer. *Nucl. Med. Commun.* **2019**, *40*, 940–946. [[CrossRef](#)] [[PubMed](#)]
16. Hasan, S.; Prelas, M.A. Molybdenum-99 production pathways and the sorbents for $^{99}\text{Mo}/^{99\text{m}}\text{Tc}$ generator systems using (n, γ) ^{99}Mo : A review. *SN Appl. Sci.* **2020**, *2*, 1782. [[CrossRef](#)]
17. Marlina; Ridwan, M.; Abdullah, I.; Yulizar, Y. Recent progress and future challenge of high-capacity adsorbent for non-fission molybdenum-99 (^{99}Mo) in application of $^{99}\text{Mo}/^{99\text{m}}\text{Tc}$ generator. *AIP Conf. Proc.* **2021**, *2346*, 030003. [[CrossRef](#)]
18. Munir, M.; Herlina; Sriyono; Sarmini, E.; Abidin; Lubis, H.; Marlina. Influence of GA Siwabessy Reactor Irradiation Period on The Molybdenum-99 (^{99}Mo) Production by Neutron Activation of Natural Molybdenum to Produce Technetium-99m ($^{99\text{m}}\text{Tc}$). *J. Phys. Conf. Ser.* **2019**, *1204*, 012021. [[CrossRef](#)]
19. Nawar, M.F.; El-Daoushy, A.F.; Ashry, A.; Türler, A. Developing a Chromatographic $^{99\text{m}}\text{Tc}$ Generator Based on Mesoporous Alumina for Industrial Radiotracer Applications: A Potential New Generation Sorbent for Using Low-Specific-Activity ^{99}Mo . *Molecules* **2022**, *27*, 5667. [[CrossRef](#)]

20. Nawar, M.F.; Türler, A. Development of New Generation of $^{99}\text{Mo}/^{99\text{m}}\text{Tc}$ Radioisotope Generators to Meet the Continuing Clinical Demands. In Proceedings of the 2nd International Conference on Radioanalytical and Nuclear Chemistry (RANC 2019), Budapest, Hungary, 5–10 May 2019.
21. Moreno-Gil, N.; Badillo-Almaraz, V.E.; Pérez-Hernández, R.; López-Reyes, C.; Issac-Olivé, K. Comparison of the sorption behavior of ^{99}Mo by Ti-, Si-, Ti-Si-xerogels and commercial sorbents. *J. Radioanal. Nucl. Chem. Artic.* **2021**, *328*, 679–690. [[CrossRef](#)]
22. Nawar, M.F.; El-Daoushy, A.F.; Madkour, M.; Türler, A. Sorption Profile of Low Specific Activity ^{99}Mo on Nanoceria-Based Sorbents for the Development of $^{99\text{m}}\text{Tc}$ Generators: Kinetics, Equilibrium, and Thermodynamic Studies. *Nanomaterials* **2022**, *12*, 1587. [[CrossRef](#)]
23. Sakr, T.M.; Nawar, M.F.; Fasih, T.; El-Bayoumy, S.; Abd El-Rehim, H.A. Nano-technology contributions towards the development of high performance radioisotope generators: The future promise to meet the continuing clinical demand. *Appl. Radiat. Isot.* **2017**, *129*, 67–75. [[CrossRef](#)] [[PubMed](#)]
24. Monir, T.; El-Din, A.S.; El-Nadi, Y.; Ali, A. A novel ionic liquid-impregnated chitosan application for separation and purification of fission ^{99}Mo from alkaline solution. *Radiochim. Acta* **2020**, *108*, 649–659. [[CrossRef](#)]
25. Van Tran, T.; Nguyen, V.H.; Nong, L.X.; Nguyen, H.-T.T.; Nguyen, D.T.C.; Nguyen, H.T.T.; Nguyen, T.D. Hexagonal Fe-based MIL-88B nanocrystals with NH_2 functional groups accelerating oxytetracycline capture via hydrogen bonding. *Surf. Interfaces* **2020**, *20*, 100605. [[CrossRef](#)]
26. Dash, A.; Chakravarty, R.; Ram, R.; Pillai, K.; Yadav, Y.Y.; Wagh, D.; Verma, R.; Biswas, S.; Venkatesh, M. Development of a $^{99}\text{Mo}/^{99\text{m}}\text{Tc}$ generator using alumina microspheres for industrial radiotracer applications. *Appl. Radiat. Isot.* **2012**, *70*, 51–58. [[CrossRef](#)] [[PubMed](#)]
27. Moret, J.; Alkemade, J.; Upcraft, T.; Oehlke, E.; Wolterbeek, H.; van Ommen, J.; Denkova, A. The application of atomic layer deposition in the production of sorbents for $^{99}\text{Mo}/^{99\text{m}}\text{Tc}$ generator. *Appl. Radiat. Isot.* **2020**, *164*, 109266. [[CrossRef](#)]
28. Reedijk, J.; Poepelmeier, K. *Comprehensive Inorganic Chemistry II: From Elements to Applications*, 2nd ed.; Elsevier Ltd.: Singapore, 2013; pp. 1–7196. [[CrossRef](#)]
29. Bernauer, U.; Bodin, L.; Chaudhry, Q.; Coenraads, P.J.; Dusinska, M.; Gaffet, E.; Panteri, E.; Rousselle, C.; Stepnik, M.; Wijnhoven, S.; et al. *SCCS Opinion on Solubility of Synthetic Amorphous Silica (SAS)-SCCS/1606/19*; Publications Office of the European Union: Luxembourg, 2020; Available online: <https://hal.archives-ouvertes.fr/hal-03115473> (accessed on 23 September 2022).
30. Ashry, A.; Bailey, E.H.; Chenery, S.R.N.; Young, S.D. Kinetic study of time-dependent fixation of U(VI) on biochar. *J. Hazard Mater.* **2016**, *320*, 55–66. [[CrossRef](#)]
31. Ashry, A. Adsorption and Time Dependent Fixation of Uranium (VI) in Synthetic and Natural Matrices. Ph.D. Thesis, University of Nottingham, Nottingham, UK, 2017.
32. Mahmoud, M.R.; Soliman, M.A.; Allan, K.F. Removal of Thoron and Arsenazo III from radioactive liquid waste by sorption onto cetyltrimethylammonium-functionalized polyacrylonitrile. *J. Radioanal. Nucl. Chem. Artic.* **2014**, *300*, 1195–1207. [[CrossRef](#)]
33. Mahmoud, M.R.; Sharaf El-deen, G.E.; Soliman, M.A. Surfactant-impregnated activated carbon for enhanced adsorptive re-moval of Ce(IV) radionuclides from aqueous solutions. *Ann. Nucl. Energy* **2014**, *72*, 134–144. [[CrossRef](#)]
34. Langmuir, I. The adsorption of gases on plane surfaces of glass, mica and platinum. *J. Am. Chem. Soc.* **1918**, *40*, 1361–1403. [[CrossRef](#)]
35. Akbas, Y.A.; Yusan, S.; Sert, S.; Aytas, S. Sorption of Ce(III) on magnetic/olive pomace nanocomposite: Isotherm, kinetic and thermodynamic studies. *Environ. Sci. Pollut. Res.* **2021**, *28*, 56782–56794. [[CrossRef](#)]
36. Alothman, Z.A.; Naushad, M.; Ali, R. Kinetic, equilibrium isotherm and thermodynamic studies of Cr(VI) adsorption onto low-cost adsorbent developed from peanut shell activated with phosphoric acid. *Environ. Sci. Pollut. Res.* **2013**, *20*, 3351–3365. [[CrossRef](#)] [[PubMed](#)]
37. Zhang, J.; Deng, R.j.; Ren, B.Z.; Hou, B.; Hursthouse, A. Preparation of a novel $\text{Fe}_3\text{O}_4/\text{HCO}$ composite adsorbent and the mechanism for the removal of antimony (III) from aqueous solution. *Sci. Rep.* **2019**, *9*, 13021. [[CrossRef](#)] [[PubMed](#)]
38. Zheng, H.; Wang, Y.; Zheng, Y.; Zhang, H.; Liang, S.; Long, M. Equilibrium, kinetic and thermodynamic studies on the sorption of 4-hydroxyphenol on Cr-bentonite. *Chem. Eng. J.* **2008**, *143*, 117–123. [[CrossRef](#)]
39. Naiya, T.K.; Bhattacharya, A.K.; Mandal, S.; Das, S.K. The sorption of lead(II) ions on rice husk ash. *J. Hazard. Mater.* **2009**, *163*, 1254–1264. [[CrossRef](#)] [[PubMed](#)]
40. Hamdaoui, O.; Naffrechoux, E. Modeling of adsorption isotherms of phenol and chlorophenols onto granular activated carbon. Part I. Two-parameter models and equations allowing determination of thermodynamic parameters. *J. Hazard Mater.* **2007**, *147*, 381–394. [[CrossRef](#)] [[PubMed](#)]